Mode conversion from quantized to propagating spin waves in a rhombic antidot lattice supporting spin wave nanochannels

S. Tacchi,[1] B. Botters,[2] M. Madami,[1] J. W. Kłos,[3] M. L. Sokolovskyy,[3] M. Krawczyk,[3] G. Gubbiotti,[1,4] G. Carlotti,[1,5] A. O. Adeyeye,[6] S. Neusser,[2] and D. Grundler[2,*]

[1]*CNISM, Unità di Perugia - Dipartimento di Fisica, Via A. Pascoli, I-06123 Perugia, Italy*

[2]*Lehrstuhl für Physik funktionaler Schichtsysteme, Physik Department, Technische Universität München, James-Franck-Str. 1, D-85747 Garching b. München, Germany*

[3]*Faculty of Physics, Adam Mickiewicz University, Umultowska 85, Poznań, 61-614, Poland*

[4]*IOM-CNR, Via Pascoli, 06123 Perugia, Italy*

[5]*Centro S3, CNR-Instituto di Nanoscienze, Via Campi 213A, I-41125 Modena, Italy*

[6]*Department of Electrical and Computer Engineering, National University of Singapore 117576, Singapore*

(Received 23 March 2012; published 17 July 2012)

We report spin wave excitations in a nanopatterned antidot lattice fabricated from a 30-nm thick $Ni_{80}Fe_{20}$ film. The 250-nm-wide circular holes are arranged in a rhombic unit cell with a lattice constant of 400 nm. By Brillouin light scattering, we find that quantized spin wave modes transform to propagating ones and vice versa by changing the in-plane orientation of the applied magnetic field **H** by 30°. Spin waves of either negative or positive group velocity are found. In the latter case, they propagate in narrow channels exhibiting a width of below 100 nm. We use the plane wave method to calculate the spin wave dispersions for the two relevant orientations of **H**. The theory allows us to explain the wave-vector-dependent characteristics of the prominent modes. Allowed minibands are formed for selected modes only for specific orientations of **H** and wave vector. The results are important for applications such as spin wave filters and interconnected waveguides in the emerging field of magnonics where the control of spin wave propagation on the nanoscale is key.

DOI: 10.1103/PhysRevB.86.014417 PACS number(s): 75.78.−n, 76.50.+g, 75.30.Ds, 75.50.Bb

I. INTRODUCTION

Spin wave (SW) modes in individual mesoscopic magnets[1] and in antidot lattices (ADLs),[2–11] i.e., thin ferromagnetic films that are periodically structured with holes, have attracted considerable interest in recent years. The dynamic response of magnetic antidots has been investigated from the GHz up to the optical frequency regime.[12,13] For antidot lattices, it has been found that the holes' edges lead not only to distinct quantization conditions for spin waves due to lateral confinement. They also generate a periodically modulated internal magnetic field H_{int} due to the demagnetization effect. In squared antidot lattices, the inhomogeneous field H_{int} has been found to provoke coexisting localized and extended modes depending on the magnetic field **H**.[12,14–19] Rhombic and honeycomb antidot lattices have so far been less investigated[20–22] and experimental data have been presented for a wave vector $q = 0$ only.[23] Considering an antidot array as a mesh of interconnected waveguides, it is interesting to study spin wave propagation and possible anisotropic behavior at $q \neq 0$. It is of particular interest whether the periodic arrangement of holes forms an artificial crystal for spin waves, i.e., a magnonic crystal (MC),[24–26] and gives rise to miniband formation as well as forbidden frequency gaps. In this paper, we investigate spin wave modes in an antidot lattice where nanostructured holes are arranged on a rhombic lattice [see Fig. 1(a)]. Using all-electrical broadband spectroscopy, Brillouin light scattering (BLS)[27,28] and micromagnetic simulations we address spin excitations for different orientations (angles ϕ) of an in-plane magnetic field. BLS is exploited to access magnetostatic surface spin waves (MSSW) and magnetostatic backward volume waves (MSBVW) with wave vectors $q \neq 0$ with the magnetic field **H** applied along high-symmetry directions of the ADL. Only specific modes are observed to exhibit positive or negative propagation velocities for $\phi = 0°$ and 30°. Propagation is found to occur, in particular, for a coherently coupled edge mode at low frequency f and in narrow channels with a width of slightly below 100 nm. We implement the plane wave method (PWM) to calculate spin wave dispersions and mode intensities to interpret the BLS data. From this, we find that allowed minibands exhibiting a periodic dispersion relation $f(q)$ in reciprocal space are formed only under specific conditions. The findings are relevant for research on magnonic crystals[25] as well as spin wave filters and waveguides based on periodically patterned nanomagnets.[24,29–32]

The paper is organized as follows: in Sec. II, we outline experimental techniques and introduce angular dependent spin wave spectroscopy data obtained at wave vector q close to zero. Basic assumptions for simulations and the PWM are discussed in Sec. III. In Sec. IV, we first explain SW excitations at $q = 0$ using micromagnetic modeling. In particular, we present the angular dependence and define the relevant high-symmetry directions (see Sec. IV A) where BLS is used to explore SW dispersion relations $f(q)$ in detail. These results are presented in Sec. IV B. Section V is devoted to the results and band structures extracted from the PWM. First, we provide the specific approximations and relevant formalism based on which we performed the calculations (see Sec. V A). Second, we compare in detail calculated dispersion relations with BLS data for specific high-symmetry directions and scattering geometries (see Sec. V B). In Sec. VI, we discuss the final outcome and conclude. Appendix addresses the block-matrix $\hat{M}$ of the eigenvalue problem.

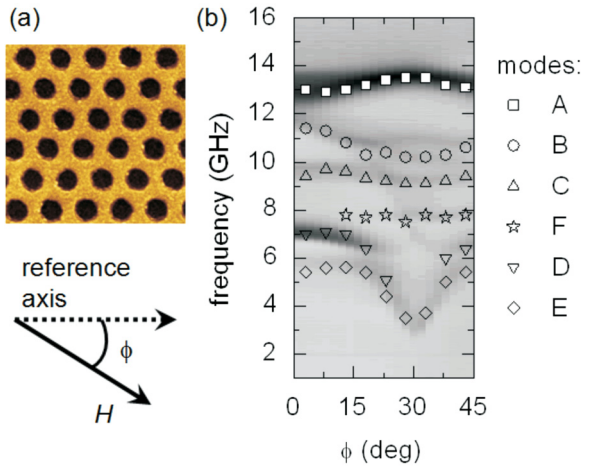

FIG. 1. (Color online) (a) Scanning electron microscopy image of the rhombic permalloy antidot lattice. The holes (black) have a diameter of 250 nm. The lattice constant is 400 nm. ϕ is the in-plane angle defined between **H** and the reference axis (broken arrow). (b) Data for $q = 0$ from Ref. 23. They have been obtained by, both, all-electrical broadband spectroscopy (gray-scale plot) and Brillouin light scattering (symbols) at different angles ϕ for $\mu_0 H = 90$ mT. Dark color encodes the excitation of eigenmodes.

II. EXPERIMENTAL TECHNIQUES AND DEFINITION OF RELEVANT FIELD AND WAVE VECTOR ORIENTATIONS

The antidot array was fabricated from a permalloy ($Ni_{80}Fe_{20}$, Py) film using optical lithography at 248-nm exposure wavelength [see Fig. 1(a)].[33] The thickness d was 30 nm. We prepared the rhombic lattice with primitive lattice vectors of length $a = 400$ nm. Before performing the BLS experiments with wave vectors $q > 0$, we used all-electrical broadband spectroscopy to explore how spin wave excitations with $q \approx 0$ depended on the direction of the in-plane magnetic field **H**.[23] In the experiment, spins were excited by placing the array on top of a coplanar waveguide (CPW) connected to a vector network analyzer (VNA) providing a continuous-wave sinusoidal output voltage with a frequency f between 10 MHz and 26 GHz.[34–36] The CPW was aligned collinearly with the reference axis using a rotatable sample holder.[37] It had an inner conductor width w of 20 μm, which was much smaller than the lateral width of the antidot array which was on the mm scale. In fact, this is a different experimental regime compared to the previously known VNA-FMR technique where the ferromagnetic resonance (FMR), i.e., uniform precession, and further *standing* spin-precessional excitations were addressed in ferromagnetic nanostructures being in particular smaller than the width of the inner conductor of the CPW.[34] For VNA-FMR experiments, the boundary conditions for spin waves in the individual ferromagnetic element and the symmetry of the excitation field are key for the excited modes. When the sample is larger than the width of the CPW, the scenario is different and the CPW transfers a specific regime of wave vectors q to the spin system that is given by the design of the CPW. Thereby, one might address *propagating* spin waves as well.[17,38] It has been shown that this leads to a characteristic broadening of the linewidth that is not relevant for the VNA-FMR experiments.[39,40] Depending on the design of the CPW, the uniform mode might not be excited.[40] [Since excited wave vectors are nonzero and depend decisively on the design of the emitter antenna (being a transmission or stripline, straight CPW, meander-type CPW, etc.), one might avoid the term VNA-FMR as the general term for such a broadband all-electrical spin wave spectroscopy technique. The term VNA-FMR might provoke confusion for nonspecialists when the uniform precession (FMR) is not excited due to the specific CPW design.[40]] In the experiment reported here, the transferred wave vector was around 0.008×10^5 rad/cm,[17] being orders of magnitude smaller than the values of q addressed in the BLS experiments outlined later. For this reason, we will refer, hereafter, to the data as being obtained at the center of the Brillouin zone (BZ) (i.e., the Γ point) and will not discuss the linewidth broadening.[39,40] The angle ϕ was varied by using correctly balanced currents in two pairs of coils generating the in-plane vector magnetic field **H**. To measure the spin wave spectra for different angles ϕ, a field of 90 mT was applied that ensured sample saturation in all the in-plane directions.[33] By this means, we observed the expected sixfold angular dependence[22] and determined the high-symmetry directions relevant for the wave-vector dependent BLS studies. We show all-electrical spin wave spectroscopy data of the relevant angular regime in Fig. 1(b) and introduce the mode labels there.

BLS from thermally excited spin waves was performed using a Sandercock type $(3+3)$-pass tandem Fabry-Perot interferometer. Laser light with a wavelength λ of 532 nm and power of 200 mW from a solid state laser was focused on the sample surface. The diameter of the laser spot was about 30 μm causing a local heating of about 40 K.[41] This temperature variation, however, did not result in an appreciable decrease of the saturation magnetization, as will be shown by the good quantitative agreement of BLS and all-electrical spin wave spectroscopy data [c.f. Fig. 1(b)].

For BLS, the sample was placed on a two-axis goniometer that allowed us to choose a specified angle of incidence of light (θ) as well as to rotate the sample around the surface normal (azimuthal rotation, ϕ). Because of the backscattering configuration used here and the conservation of momentum in the scattering process, the magnitude of the in-plane transferred wave vector q depended on the incidence angle of light θ according to $q = (4\pi/\lambda)\sin\theta$. The angle θ was defined with respect to the sample normal. The wave vectors addressed in the BLS experiments ranged from 0 to 2.0×10^5 rad/cm by varying θ from 0° to 60°, respectively. It should be noticed that the maximum transferred wave vector was beyond the boundary of the first BZ of the rhombic antidot lattice with a primitive vector of length $a = 400$ nm. For $q > 0$ data, we focus on $\phi = 0°$ and 30° with two different relative orientations between **q** and **H** corresponding to either the MSBVW geometry (where **q** is parallel to **H**) or the MSSW geometry (where **q** is perpendicular to **H**).

III. SIMULATIONS AND THEORETICAL APPROACH

A. Micromagnetic modeling

The commercial software package MICROMAGUS[42] was used to calculate the static magnetization pattern as well as the mode eigenfrequencies and spatial profiles of spin precession

amplitudes at $q = 0$. Two-dimensional (2D) periodic boundary conditions were applied. Parameters were a cell size of $6 \times 6 \times 30\,\mathrm{nm}^3$ (30 nm is valid for the out-of-plane direction), saturation magnetization of 827 kA/m, exchange (damping) constant of 1.3×10^{-11} J/m (0.01). These parameters are consistent with Ref. 23. To explore excitations with $q = 0$, a homogeneous field pulse $\mu_0 h_{\mathrm{rf}}$ of 3-ps duration and amplitude of 4 mT was applied, directed 45° out of the plane. This was done to excite several SW modes of different symmetry.

B. The plane wave method

The band structures of spin wave excitations (frequency versus wave vector q) in materials with discrete translational symmetry, including electronic, photonic, phononic, and magnonic crystals, can be calculated by the PWM. This method is a popular tool because of its conceptual simplicity and its applicability to any type of lattice and any shape of scattering centers.[43–47] The method is being constantly improved, with its field of application extending to new problems,[47–49] like the calculation of the spin wave spectra of one-dimensional (1D) and 2D MCs of finite thickness.[50,51] This requires the inhomogeneity of the internal magnetic field to be taken into account in the calculations. The PWM has been employed in Ref. 11 for calculating the spin wave spectra of 2D ADLs based on a square lattice for the first time. Here, we apply the same technique to a 2D ADL having a rhombic lattice considering the above defined MSSW and MSBVW geometries.

In the classical approach, the spin wave dispersion relation is determined from the Landau-Lifshitz (LL) equation, i.e., the equation of motion of the magnetization vector $\mathbf{M}(\mathbf{r},t)$:

$$\frac{\partial \mathbf{M}(\mathbf{r},t)}{\partial t} = \gamma \mu_0 \mathbf{M}(\mathbf{r},t) \times \mathbf{H}_{\mathrm{eff}}(\mathbf{r},t), \tag{1}$$

where γ is the gyromagnetic ratio, $\mathbf{H}_{\mathrm{eff}}$ denotes the effective magnetic field acting on the magnetic moments, and $\mathbf{r}$ and t are the spatial and time coordinates, respectively. Equation (1) applies to the case of negligible relaxation. It is expressed in SI units, used throughout this paper, with μ_0 denoting the permeability of vacuum. We assume $\gamma\mu_0 = -2.21 \times 10^5\ (\mathrm{A/m})^{-1}\mathrm{s}^{-1}$.

A uniform static magnetization in the magnetic material of the ADL is assumed, allowing us to use the linear approximation and a global coordinate system in which the y and z axes define the plane of periodicity, and the x axis is normal to the surface of the ADL. In our calculations, the static magnetic field is assumed to be oriented always along the z axis [c.f. Fig. 5(a)]. In the linear approximation, the component $M_z(\mathbf{r})$ of the magnetization vector parallel to the static magnetic field is constant in time, and its magnitude is much greater than that of the perpendicular components $\mathbf{m}(\mathbf{r},t)$: $|\mathbf{m}(\mathbf{r},t)| \ll M_z(\mathbf{r})$ with $\mathbf{M}(\mathbf{r},t) = M_z(\mathbf{r})\hat{z} + \mathbf{m}(\mathbf{r},t)$ ($\hat{x}$, $\hat{y}$, and $\hat{z}$ are unit vectors). Thus we can assume $M_z \approx M_{\mathrm{S}}$, M_{S} being the saturation magnetization, and neglect all the terms with squared $\mathbf{m}(\mathbf{r},t)$ and dynamical components of $\mathbf{H}_{\mathrm{ms}}(\mathbf{r},t)$ (defined below). We search only for solutions of Eq. (1) corresponding to monochromatic spin waves: $\mathbf{m}(\mathbf{r},t) \sim \exp(i\omega t)$, $\omega = 2\pi f$ being the wave frequency.

The effective magnetic field $\mathbf{H}_{\mathrm{eff}}$ acting on the magnetic moments is, in general, the sum of several components. However, here we consider only three contributions: a uniform and constant applied magnetic field $\mathbf{H}$ (applied along the z axis), the exchange field $\mathbf{H}_{\mathrm{ex}}$ and the magnetostatic field $\mathbf{H}_{\mathrm{ms}}$. The latter two, i.e., the exchange field and the magnetostatic field, are space and time dependent:

$$\mathbf{H}_{\mathrm{eff}}(\mathbf{r},t) = \mathbf{H} + \mathbf{H}_{\mathrm{ex}}(\mathbf{r},t) + \mathbf{H}_{\mathrm{ms}}(\mathbf{r},t). \tag{2}$$

The magnetostatic field provides one of the main challenges in spin wave calculations in magnetic systems. We decompose this field into the static and dynamic components, $\mathbf{H}_{\mathrm{ms}}(\mathbf{r})$ and $\mathbf{h}_{\mathrm{ms}}(\mathbf{r},t)$, respectively. The time dependence of the dynamic magnetostatic field has the same form as that of the dynamic component of the magnetization vector: $\mathbf{h}_{\mathrm{ms}}(\mathbf{r},t) = \mathbf{h}_{\mathrm{ms}}(\mathbf{r})e^{i\omega t}$. The geometrical structure and magnetic configuration of the ADL imply special approximations to be used. We will discuss these approximations later in detail in Sec. V A after presenting relevant results from micromagnetic simulations and BLS experiments in the next section.

IV. EXPERIMENTAL RESULTS AND MICROMAGNETIC MODELING

A. Excitations for zero wave vector: angular dependence and spin-precession profiles

Before discussing the wave-vector dependent BLS data and dispersion relations $f(q)$ for specific high symmetry directions it is instructive to analyze the dependence of SWs with $\mathbf{q} = 0$ (i.e., at the Γ point) on the in-plane angle ϕ of the applied magnetic field [as defined in Fig. 1(a)]. For this, we perform all-electrical broadband spectroscopy and BLS at $q = 0$ for different ϕ. Numerous eigenmodes are found that exhibit a sixfold rotational symmetry.[22,23] Relevant data are contained in Fig. 1(b) in the angular regime between $\phi = 0°$ and 45°. Dark color encodes the excitation of eigenmodes, i.e., an absorption signal in the CPW due to spin precession in the ADL. The symbols in Fig. 1(b) represent the BLS data taken at $\theta = 0°$, i.e., $q = 0$, and they are labeled from A to E. We observe a very good agreement with the all-electrical broadband spectroscopy data. Mode F is additionally observed in the BLS experiment. The PWM provides even more modes as will be detailed later. In Fig. 2(a), we show the field dependence as obtained from micromagnetic simulations for $q = 0$.[23] Figures 2(b)–2(d) depict relevant spin precession profiles to illustrate the different excitations. The spin precession profiles reflect different kinds of modes either being localized in specific regions or extending through the lattice in a nearly stripelike manner [broken lines in Figs. 2(b) to 2(d)]. The direction of the stripes depends on both the eigenfrequency and the orientation of $\mathbf{H}$.

The most intense peaks of the BLS spectra at $\phi = 0°$ belong to modes A and D. The images presented in Figs. 2(b) and 2(c) for $\phi = 0°$ show that the modes reside mainly between nearest (mode A) and next-nearest (mode D) neighboring holes at $\phi = 0$. Mode D shows a localized nature and is quantized in two spatial directions by the existing holes whereas mode A has an extended character along the field

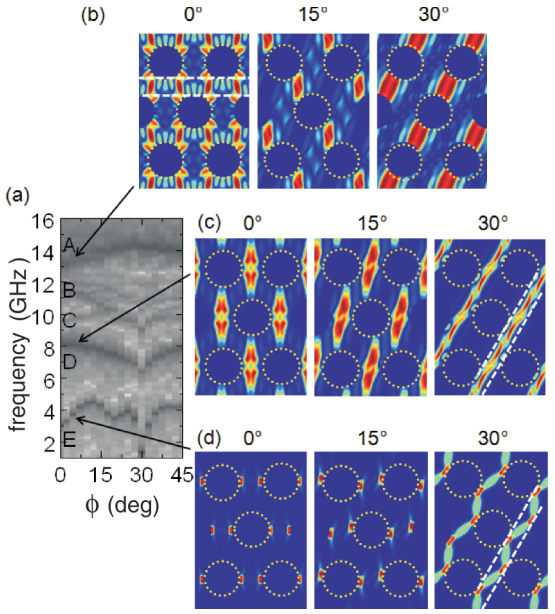

FIG. 2. (Color online) (a) Excitation spectra at $q = 0$ simulated as a function of ϕ at $\mu_0 H = 90$ mT. Dark color encodes eigenfrequencies. Local spin-precession amplitudes for modes (b) A, (c) D, and (d) E. The spatial spin-precession profiles are shown for three different angles $\phi = 0°, 15°$, and $30°$ as labeled on the top (from left to right). Dark (bright) encodes zero (maximum) precession amplitude. Dashed lines highlight stripelike precession profiles extending through the lattice.

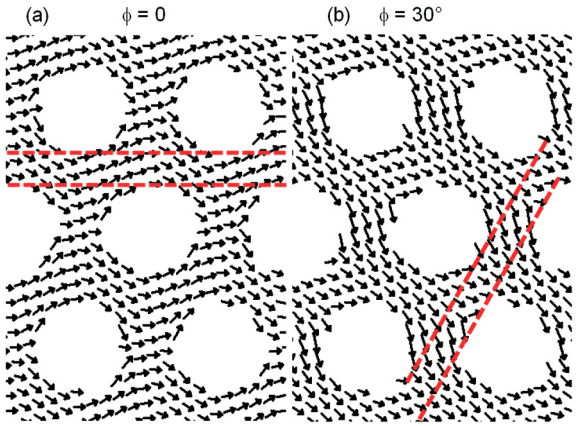

FIG. 3. (Color online) Simulated magnetic configurations of the antidot lattice for $\mu_0 H = 90$ mT applied under an angle of (a) $\phi = 0°$ and (b) $30°$. Arrows illustrate the local orientation of the microscopic magnetic moments averaged over several simulation cells for clarity. The dashed lines reflect the 96-nm-wide stripes defined in Figs. 2(b) to 2(d).

direction. This is highlighted by the dashed horizontal lines in Fig. 2(b). Its spatial distribution (standing wave profile) strongly oscillates because of the hybridization with other modes. Large spin precession amplitudes of mode A are found mainly in stripes where the field H_{eff} is large, i.e., the demagnetization effect originating from the holes is weak compared to the regions where mode D exhibits large spin-precession amplitudes. This explains to a large amount the large eigenfrequency of mode A compared to mode D. Relating the spin-precession profiles of Figs. 2(b) and 2(c) at $\phi = 0°$ with the magnetic configuration shown in Fig. 3(a), we find that both modes exhibit large spin-precession amplitudes in regions where the local magnetic moments tend to align with the applied field. The demagnetization effect of the holes, however, prevent the moments from being strictly collinear with **H**.

Considering the dashed horizontal lines in Fig. 2(b) the width of a stripe amounts to $400\text{ nm} \times \sin(60°) - 250\text{ nm} = 96$ nm. The corresponding magnetic configuration displayed in Fig. 3(a) resembles a magnetic nanowire that is magnetized in *longitudinal* direction. Due to the holes the microscopic magnetic moments follow, however, a wavy pattern.

When the direction of the external field is rotated to $\phi = 15°$, the mode profiles shift. Large spin precession amplitudes remain in the regions where the static magnetization tends to align with the field. Mode A, however, does not show an extended character along the field direction any longer, and, increasing ϕ further, it clearly localizes between nearest-neighboring holes at $\phi = 30°$ [see Fig. 2(b), right]. The opposite evolution with increasing ϕ is observed for modes D and E. Initially localized at $\phi = 0°$, modes D and E get an extended character at $\phi = 30°$ [see Fig. 2(c), right]. The large spin-precession amplitudes occur along stripes perpendicular to **H** which are enclosed by holes. The stripes (between dashed lines) have again a width of 96 nm. Considering the magnetic configuration displayed in Fig. 3(b), these stripes resemble magnetic nanowires, which are magnetized in *transverse* direction, and thereby experience a small field H_{eff}. Again, a wavy pattern of the magnetization M is superimposed due to the holes.

Interestingly, the low-frequency mode E corresponds to a so-called edge mode [see Fig. 2(d)]. For this mode, large spin-precession amplitudes occur in spin wave wells,[1] i.e., local minima of H_{eff} generated by stray fields right at the edges of holes. At $\phi = 0°$ and $\phi = 15°$ in Fig. 2(d) the edge excitations exhibit large spin precession amplitudes only at opposing edges of holes. Tilting ϕ moves these local amplitude maxima in space. At $\phi = 30°$ in Fig. 2(d), large amplitudes are found also in-between holes forming a zigzaglike shape of the spin-precession profile. The zigzaglike shape is along the stripe marked by dashed lines in Fig. 2(d) at $\phi = 30°$. Here, edge excitations couple from edge to edge. The eigenfrequency given by the micromagnetic simulation at this angle is too small [see Fig. 2(a)] compared to the experimental data [see Fig. 1(b)]. For the simulation, we have assumed hole edges that are almost perfect, i.e., the edges are rough only on the lateral scale of the implemented cell size. A cubic-shaped simulation cell covers an area of 6×6 nm^2 in the plane of the magnetic film. This small residual roughness is in particular deterministic throughout the lattice due to the 2D periodic boundary conditions. In contrast to this, the roughness in the real sample is larger as seen in Fig. 1 and irregular, i.e., it varies from hole to hole. The discrepancies between simulated and experimental eigenfrequencies of mode E are attributed to imperfections of the real antidot lattice modifying the internal field.[57]

From the data in Figs. 1(b) and 2, we extract that the two angles $\phi = 0^\circ$ and 30° are, in particular, interesting. For these two specific angles, mode A (E) exhibits its local frequency minimum and maximum (maximum and minimum), respectively. The dispersion relations obtained by both BLS and PWM for these angles will be presented and discussed in the next sections.

B. Brillouin light scattering for $q \neq 0$

In the upper row of Fig. 4, we define the different scattering geometries used in the present study [see Figs. 4(a), 4(d), 4(g), and 4(j)]. In the center row, we depict corresponding BLS spectra in Figs. 4(b), 4(e), 4(h), and 4(k).[58] In the bottom row [see Figs. 4(c), 4(f), 4(i), and 4(l)], we summarize the spin wave eigenfrequencies as a function of q. We report BLS data for frequencies f being smaller than the first-order perpendicular standing spin wave mode occurring at 21 GHz. It can be seen that, remarkably, many modes exhibit a constant eigenfrequency and do not depend on q, i.e., the group velocity $v_g = d(2\pi f)/dq$ is zero. Such a strong suppression of spin wave propagation and quantization of spin waves are different from square lattices investigated recently.[17] However, such effects might be expected if one considers the rhombic lattice to be equivalent with a rectangular lattice that incorporates an additional hole in the unit-cell center. The additional hole reduces the $Ni_{80}Fe_{20}$ filling fraction[17] to a small number and fosters a high degree of quantization. However, mode A in the MSBVW geometry [see Fig. 4(c)] and mode E in the MSSW geometry [see Fig. 4(l)] clearly have a finite slope as a function of q, i.e., a dispersive behavior. In Fig. 4(c), we observe that the eigenfrequency of mode A decreases with increasing q. The corresponding group velocity extracted near $q = 0$ is $v_g \approx -0.7$ km/s. A negative slope is known from a MSBVW in a continuous permalloy film. For increasing wave vector q, the absolute value of the group velocity is found to decrease. This behavior is known from a MSBVW in a continuous film up to the crossover from dipolar to exchange-dominated modes. This crossover takes place with increasing wave vector q. For the three other scattering geometries studied below, mode A shows a constant eigenfrequency (within the error bar) as a function of q [see Figs. 4(f), 4(i), and 4(l)]. In Fig. 4(c), mode E has first an almost constant frequency up to about 1×10^5 rad/cm and then splits into a doublet. The upper branch of this doublet is characterized by a slightly positive group velocity, while the latter one (E_{AS}) by a negative value. The wave vector 1×10^5 rad/cm is close to the boundary of the first BZ.

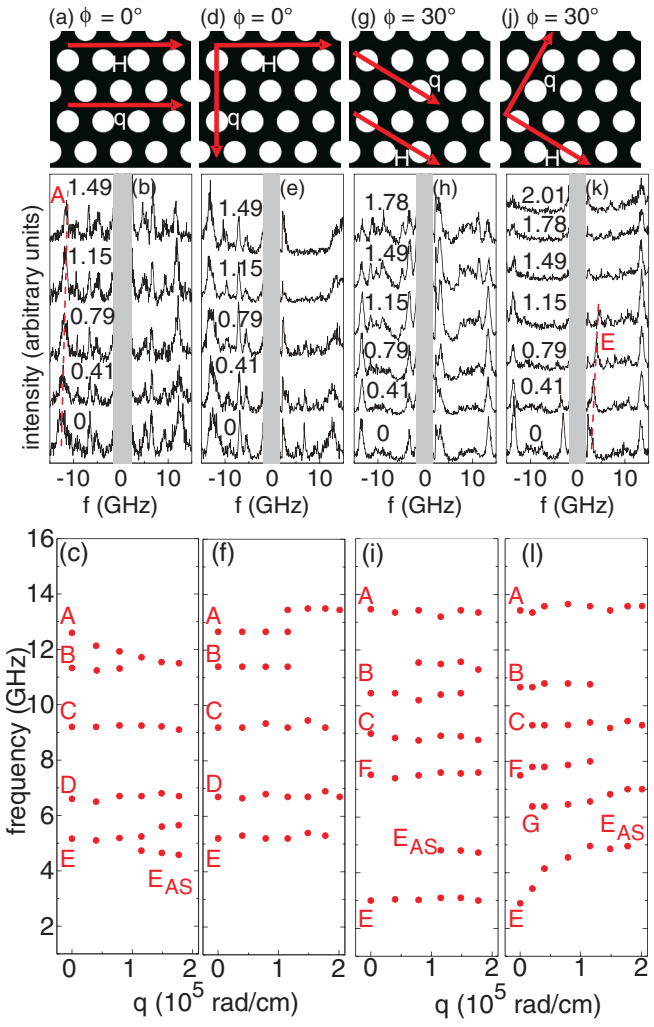

FIG. 4. (Color online) Each column reflects a specific scattering geometry as illustrated in (a), (d), (g), and (j). (b), (e), (h), and (k) Sequences of BLS spectra for $\mu_0 H = 90$ mT taken at different values of the in-plane transferred wave vector q in the scattering geometries depicted above. The numbers denote the values of q in units of 10^5 rad/cm. Broken lines interconnect peaks reflecting the same eigenmode as labeled. In (c), (f), (i), and (l), we show the spin wave frequencies as extracted from the corresponding BLS spectra and summarize them as a function of q. The values q go beyond the boundary of the first BZ as indicated in Fig. 5(b). Broken lines are guides to the eyes. Gray-shaded areas indicate regimes where BLS spectra are not evaluated due to stray light.

Turning to the MSSW geometry [see Fig. 4(l)], it can be seen that the frequency of mode E increases with a positive slope up to 1×10^5 rad/cm and then becomes almost flat. The slope at small q corresponds to $v_g \approx 2.2$ km/s. This value is comparable to typical group velocities ranging from 2 to 4 km/s found for propagating modes in squared ADLs of large $Ni_{80}Fe_{20}$ filling fraction.[11,17] For further scattering geometries, mode E is nearly constant with q [see Figs. 4(f) and 4(i)].

Interestingly, in the rhombic lattice, a mode that is propagating for $\phi = 0$ (mode A) becomes quantized for 30° and vice versa (mode E). Such an opposing mode conversion has not been reported for the squared antidot lattices.

V. BAND STRUCTURES AND WAVE-VECTOR-DEPENDENT SPIN PRECESSION PROFILES FROM THE PLANE WAVE METHOD

A. Specific approximations and the PWM formalism for a rhombic lattice

In the PWM calculations, we assume that the applied magnetic field is strong enough to enforce a parallel alignment of all the magnetic moments. Limitations of this approach will be discussed later. The exchange field is assumed to have the

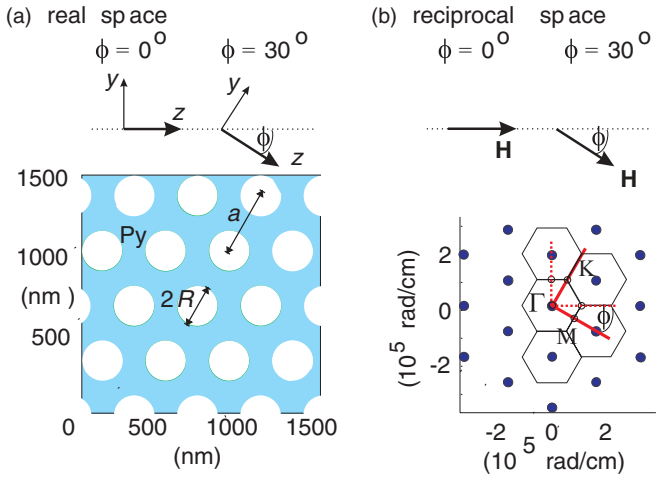

FIG. 5. (Color online) (a) Rhombic-lattice based ADL considered in this study. Antidots are represented by white holes with radius R. For the PWM, we assume the magnetic field to be always oriented along the z axis, i.e., in the $\phi = 0°$ geometry along the horizontal line and in the $\phi = 30°$ geometry along the line clockwise-rotated by 30°. For the PWM, we thus rotate the in-plane components of the coordinate system consistent with a rotation of the magnetic field. The x direction points out of the plane. (b) Reciprocal space for the structure shown in (a) with indicated high-symmetry points Γ, K, and M in the center and at the border of the first BZ, respectively. Solid (dotted) lines represent the wave-vector range studied in BLS experiments, i.e., from 0 to 2.0×10^5 rad/cm along **H** and perpendicular to **H** in $\phi = 30°$ ($\phi = 0°$) geometry.

form that can be obtained directly from the exchange-energy functional in the linear approximation:

$$\mathbf{H}_{\mathrm{ex}}(\mathbf{r},t) = \left(\nabla \cdot l_{\mathrm{ex}}^2(\mathbf{r},t)\nabla\right)\mathbf{m}(\mathbf{r},t), \tag{3}$$

$$\text{where} \quad l_{\mathrm{ex}} = \sqrt{\frac{2A}{\mu_0 M_{\mathrm{S}}^2}}. \tag{4}$$

In magnetically inhomogeneous materials the spatial inhomogeneity of both the exchange constant $A(\mathbf{r})$ and the spontaneous magnetization $M_{\mathrm{S}}(\mathbf{r})$ must be taken into account in the definition of the exchange field.

Crucial for the magnonic nature of the considered structure is the assumption that the material parameters in the above equations, namely, A and M_{S}, and, consequently, also l_{ex}^2, are periodic functions of the in-plane (parallel-plane) position vector $\mathbf{r} = (y,z)$, with a period equal to the lattice vector **a**.

In MCs composed of two materials, each of these material parameters can be expressed by two terms, $M_{\mathrm{S,A}}$, $M_{\mathrm{S,B}}$ and A_{A}, A_{B}, representing its respective values in each of the constituent materials. In the case of the ADL considered in this study, $M_{\mathrm{S,A}}$ refers to the air holes and is set to a small value close to zero (see below). $M_{\mathrm{S,B}}$ refers to permalloy. The lattice vector **a** in a rhombic lattice is a superposition of two primitive vectors: at $\phi = 0°$, we consider $\mathbf{a}_1 = a\hat{z}$, $\mathbf{a}_2 = a/2(\sqrt{3}\hat{y} - \hat{z})$. At $\phi = 30°$, the primitive vectors read $\mathbf{a}_1 = a\hat{y}/2 + \sqrt{3}a\hat{z}/2$ and $\mathbf{a}_2 = a\hat{y}/2 - \sqrt{3}a\hat{z}/2$, where a is the lattice constant [see Fig. 5(a)].

To solve Eq. (1), we will use Bloch's theorem, which asserts that a solution of a differential equation with periodic coefficients can be represented as a product of a plane-wave envelope function and a periodic function:

$$\mathbf{m}(\mathbf{r}) = \sum_{\mathbf{G}} \mathbf{m}_{\mathbf{q}}(\mathbf{G}) e^{i(\mathbf{q}+\mathbf{G})\cdot\mathbf{r}}, \tag{5}$$

where $\mathbf{G} = (G_y, G_z)$ denotes a reciprocal lattice vector of the considered structure; in the case of the rhombic lattice, we get for $\phi = 0$ $\mathbf{G} = \frac{2\pi}{a}(\frac{2n_y - n_z}{\sqrt{3}}, -n_z)$ and for $\phi = 30°$, $\mathbf{G} = \frac{2\pi}{a}(n_y, (2n_z - n_y)/\sqrt{3})$; n_y, and n_z are integers. The Bloch wave vector $\mathbf{q} = (q_y, q_z)$ refers to those spin waves that, according to Bloch's theorem, can be limited to the first BZ. The reciprocal lattice of the rhombic structure is shown in Fig. 5(b). The M and K points are at the boundary of the first BZ. The M point is in a distance of $2\pi/(a\sqrt{3}) = 0.907 \times 10^5$ rad/cm from the BZ center (Γ point) and the K point is in a distance of $4\pi/3a = 1.05 \times 10^5$ rad/cm from the BZ center. The solid (dotted) lines along two orthogonal directions represent the wave-vector range studied in BLS experiments for the $\phi = 30°$ ($\phi = 0°$) geometry. The maximum value q of the BLS experiment goes beyond the boundary of the first BZ as noted above. ϕ is the angle between bias magnetic field **H** and the dotted horizontal line in the structure presented in Fig. 5(a).

In the next step, we perform the Fourier transformation to map the periodic functions M_{S} and l_{ex}^2 in Eq. (1) to the reciprocal space. The transformation formulas are

$$M_{\mathrm{S}}(\mathbf{r}) = \sum_{\mathbf{G}} M_{\mathrm{S}}(\mathbf{G}) e^{i\mathbf{G}\cdot\mathbf{r}}, \tag{6}$$

$$l_{\mathrm{ex}}^2(\mathbf{r}) = \sum_{\mathbf{G}} l_{\mathrm{ex}}^2(\mathbf{G}) e^{i\mathbf{G}\cdot\mathbf{r}}. \tag{7}$$

In the case of circular antidots, the Fourier components of the saturation magnetization $M_{\mathrm{S}}(\mathbf{G})$ and the squared exchange length $l_{\mathrm{ex}}^2(\mathbf{G})$ can be calculated analytically. The formula for the saturation magnetization reads

$$M_{\mathrm{S}}(\mathbf{G}) = \begin{cases} (M_{\mathrm{S,A}} - M_{\mathrm{S,Py}})\frac{2\pi R^2}{\sqrt{3}a^2} - M_{\mathrm{S,Py}}, & \text{for } \mathbf{G} = 0, \\ (M_{\mathrm{S,A}} - M_{\mathrm{S,Py}})2\frac{2\pi R^2}{\sqrt{3}a^2}\frac{J_1(GR)}{GR}, & \text{for } \mathbf{G} \neq 0, \end{cases} \tag{8}$$

where J_1 is a Bessel function of the first kind, R is the radius of a hole, $M_{\mathrm{S,Py}}$ is the saturation magnetization of Py, and $M_{\mathrm{S,A}}$ is the nonzero magnetization, which we intentionally attribute to the holes. A nonzero value is needed for the convergence of the PWM. We take a magnetization at least ten times lower than $M_{\mathrm{S,Py}}$.[59] The formula for $l_{\mathrm{ex}}^2(\mathbf{G})$ has the same form.

We need formulas for the static and dynamic demagnetizing fields, $H_{\mathrm{ms},z}(\mathbf{r},x)$, $h_{\mathrm{ms},x}(\mathbf{r},x)$, and $h_{\mathrm{ms},y}(\mathbf{r},x)$, to finalize the formalism, in which an eigenvalue problem in the reciprocal space is derived from Eq. (1). The details of derivation and formulas for $H_{\mathrm{ms},z}(\mathbf{r},x)$, $h_{\mathrm{ms},x}(\mathbf{r},x)$, and $h_{\mathrm{ms},y}(\mathbf{r},x)$ can be found in Ref. 11 [see Eqs. (5)–(7) there]. Because the slab is thin enough (which is the case of the considered ADL structure with $d = 30$ nm), the nonuniformity of the demagnetizing field across its thickness can be neglected, and the value of the respective demagnetizing field for $x = 0$ will be used in the PWM calculations.

The substitution of the Eqs. (5)–(8) and Eqs. (5)–(7) from Ref. 11 into Eq. (1) leads to the algebraic eigenvalue problem

with eigenvalues $i\omega/\gamma\mu_0 H$:

$$\hat{M}\mathbf{m_q} = i\frac{\omega}{\gamma\mu_0 H}\mathbf{m_q}, \tag{9}$$

where the eigenvector reads

$$\mathbf{m_q^T} = [m_{x,\mathbf{q}}(\mathbf{G}_1), \cdots, m_{x,\mathbf{q}}(\mathbf{G}_N), m_{y,\mathbf{q}}(\mathbf{G}_1), \cdots, m_{y,\mathbf{q}}(\mathbf{G}_N)], \tag{10}$$

when a finite number N of reciprocal lattice vectors is used in the Fourier series of Eqs. (5) and (7). The elements of the matrix $\hat{M}$ are specified in Appendix.

We solve the system of equations defined by Eq. (9) using standard numerical procedures designed for solving complex matrix eigenvalue problems. All the eigenvalues found by these procedures must be tested for convergence, though. A satisfactory convergence of numerical solutions of Eq. (9) for all the structures considered proves to be assured by the use of 1681 reciprocal lattice vectors.

A remark must be made on the application of the PWM to the calculation of the magnonic band structures of ADLs with nonmagnetic inclusions such as holes. The difficulties lie in the very formulation of the equations of motion (the LL equation) for inhomogeneous media. The LL equation describes the dynamics of the magnetization vector in magnetic materials; in nonmagnetic media the magnetization is zero, and the LL equation becomes undefined. This implies the occurrence of nonphysical solutions, describing the dynamic components of the magnetization vector in the nonmagnetic material, in the total set of solutions.

In the ADL under consideration, the static magnetization cuts across the borders between a ferromagnet and a nonmagnetic material. This results in an inhomogeneous static demagnetizing field, locally reducing the magnetic field in the magnetic material. At the same time, the stray field substantially increases the value of the internal magnetic field in the holes. This can be observed in Figs. 6(a) and 6(c), where the component $H_{\mathrm{dem,z}}$ of the static demagnetizing field parallel to $\mathbf{H}$ is shown as a color-coded map. We consider the ADL in the two configurations $\phi = 0^\circ$ [see Fig. 6(a)] and $\phi = 30^\circ$ [see Fig. 6(c)]. In other words, the stray field shifts up the nonphysical solutions to higher frequencies. The exact frequency range in which the nonphysical solutions occur depends on the structure of the ADL and the ferromagnet. If the shift is not sufficient to push away the nonphysical solutions, a further shift in frequency is required. For this purpose, we propose the introduction of an inhomogeneous field of uniaxial anisotropy along the direction of the applied magnetic field. With assumed values being bigger than 1 T in the hole region and 0 T in the magnetic material, the uniaxial anisotropy field shifts the nonphysical solutions far enough, above 16 GHz, while the frequencies of the other solutions remain unaffected.

In Figs. 6(b) and 6(d) we show the component of the static demagnetizing field $H_{\mathrm{dem,y}}$ (perpendicular to H) calculated from formulas derived in the same way as $H_{\mathrm{dem,z}}$ in Eq. (5) in Ref. 11. The regions of the ADL with maximum and minimum values of $H_{\mathrm{dem,y}}$ correspond to the regions where the direction of the static magnetization can deviate from the saturated state assumed in the PWM formalism. Neglecting the nonuniform static magnetic field perpendicular to $\mathbf{H}$ is justified for, both, strong external fields that saturate the ADL and those SW

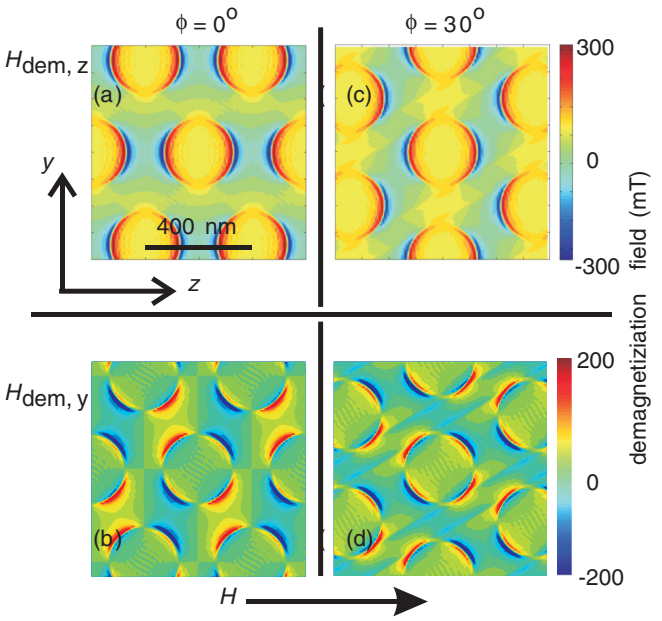

FIG. 6. (Color online) Components $H_{\mathrm{dem,z}}$ (upper row) and $H_{\mathrm{dem,y}}$ (lower row) of the static demagnetizing field calculated according to Eq. (5) from Ref. 11 in an ADL for the two different orientations of $\mathbf{H}$ with respect to the crystallographic structure: (a) and (b) $\phi = 0^\circ$ (left column) and (c) and (d) $\phi = 30^\circ$ (right column). Negative values of H_{dem} in the upper row are opposite to the bias field $\mathbf{H}$, which is assumed to point in the horizontal direction for all panels. Note that the lattice is rotated by 30° between the left and right columns. For these graphs, $\mathbf{H}$ is always in horizontal direction and the ADL is rotated.

modes that have large precession amplitude concentrated in the regions with negligible $H_{\mathrm{dem,y}}$, e.g., for the edge modes. It means also that PWM results for the SWs that have precession amplitudes spread across the ADL can be used only for the qualitative interpretation of the experimental results.

We performed calculations for the 30-nm-thick ADL made of Py with a rhombic arrangement of holes [see Fig. 5(a)]. The lattice constant was taken to be $a = 400$ nm. To obtain agreement with experimental results, especially for the edge modes, we had to increase the radius of the holes to the value $R = 130$ nm. It was 4% larger than the nominal value. For the PWM calculations, we used $M_S = 800$ kA/m and $A = 1.0 \times 10^{-11}$ J/m. We note that the magnetic parameters used in the PWM to remodel the wave-vector-dependent BLS data differed by 3% (M_S) and 30% (A) from the parameters taken for the micromagnetic simulations valid at $q = 0$. The value of the exchange constant was, in particular, relevant to account for the wave vector dependence at large q, which was not relevant for Ref. 23 and the micromagnetic simulations in Fig. 2. To model the q-dependent BLS data in the present manuscript, we needed to refine the value of A. We considered $\mu_0 H = 90$ mT being directed along the z axis. To address the two configurations studied in the experiments ($\phi = 0^\circ$ and 30°), we rotated the ADL including the in-plane components of the coordinate system while the bias field remained in the same direction [see Fig. 5(a)].

The solution of Eq. (9) yields both eigenfrequencies ω and eigenvectors $\mathbf{m_q}$. The latter are the Fourier coefficients of the dynamic magnetization components. Spatial profiles of

these components can be determined on the basis of Bloch's theorem [see Eq. (5)] and the eigenvectors $\mathbf{m_q}$ found for a given $\mathbf{q}$. When the eigenvectors in Eq. (5) are known the relative intensities of BLS spectra for different angles of the incident light can be calculated.[52] For propagating SWs, only the perpendicular-to-the-ADL-film component of the dynamical magnetization $m_x(\mathbf{r}) \propto e^{i(\mathbf{q}\cdot\mathbf{r}+\omega t)}$ will contribute to the inelastic light scattering process at the incident angle of the light which determines the wave vector $\mathbf{q}$. If the investigated spin wave mode is described by a mode profile $\mathbf{m}(\mathbf{r})$, the intensity I is determined by the Fourier component $m_x(\mathbf{q})$ of the mode:

$$I \propto |m_x(\mathbf{q})|^2. \tag{11}$$

This means that the square of the modulus of the fundamental harmonics $m_x(\mathbf{q})$ is proportional to the signal strength detected by BLS.[16] [The formula does not consider microscopic details of the inelastic light scattering process itself and thus does not account for asymmetries encountered experimentally between Stokes and anti-Stokes processes in BLS (c.f. Fig. 4).] In this description, $\mathbf{q}$ does not need to be limited to the first BZ and can span over any point of the reciprocal space. The range of wave vectors investigated in this study are marked by solid and dashed lines in Fig. 5(b). In Eq. (11), we do not take into account both the asymmetry of the efficiency of the magneto-optical interactions and the contribution of the in-plane component of the magnetization vector.

In the next section, we will show the results of the PWM calculations for $\phi = 0°$ and $\phi = 30°$. In both cases, the two relevant wave vector directions are addressed according to the MSBVW ($\mathbf{q}\|\mathbf{H}$) and MSSW ($\mathbf{q} \perp \mathbf{H}$) geometries. The magnonic band structures, measured BLS intensities and calculated spin-precession profiles are discussed for each scattering geometry at the two different angles ϕ.

B. Comparison between BLS results and PWM calculations

For $\phi = 30°$, the magnonic band structure does not exhibit mirror symmetry at the border of the first BZ for wave vectors perpendicular to $\mathbf{H}$, i.e., along q_y shown by the solid line in Fig. 5(b). Note that the paths in the BZ from Γ to K point ($q_y \approx 1.05 \times 10^5$ rad/cm) and beyond K point are not equivalent. This is contrary to the propagation along the z axis (along $\mathbf{H}$). In this case there is mirror symmetry in the magnonic band structure. The two different symmetries are reflected in PWM results and in BLS spectra.

1. MSSW geometry for $\phi = 30°$ with $q_y \neq 0$

For the MSSW geometry with $\phi = 30°$, the magnonic band structure and relative BLS intensities calculated by the PWM are shown in Figs. 7(a) and 7(c), respectively. In Fig. 7(a), the PWM results (lines) are superimposed on the BLS data (circles). Magnonic bands with predicted large scattering cross sections are emphasized by bold lines. In agreement with BLS data, the intensity of the low-frequency edge mode, i.e., mode E, disappears at the border of the first BZ [K point in Fig. 5(b)] where mode E_{AS} starts to be visible. From the calculated spin-precession amplitudes [see Fig. 7(b)], we see that two modes E and E_{AS} are edge modes with in-phase (symmetric)

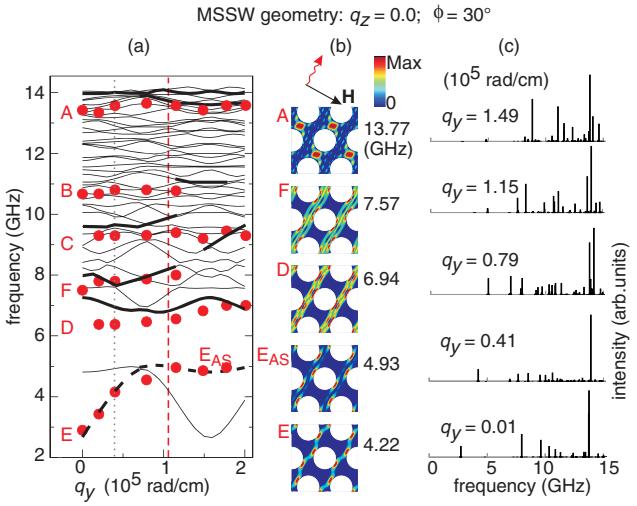

FIG. 7. (Color online) (a) Magnonic band structure in MSSW geometry for $\phi = 30°$ ($q_z = 0$). Circles represent peaks in BLS spectra. Thin lines are PWM results. Bold and dashed bold lines emphasize intense excitations as predicted by PWM. The vertical dashed line marks the border of the first BZ (i.e., the K point) while the dotted line indicates the q vector where spin-precession profiles of panel (b) have been calculated. (b) Maps show spin-precession profiles, i.e., modulus of the amplitude of the component m_x of the dynamic magnetization, for $q_y = 0.41 \times 10^5$ rad/cm. We display the most intense modes E, E_{AS}, D, F, and A. Modes E and E_{AS} are edge modes. Mode A has a spin-precession profile resembling mode A found in the micromagnetic simulations. (c) Relative values of BLS intensities as calculated by PWM for different values of q_y given in units of 10^5 rad/cm. The intensities of E and E_{AS} modes interchange at $q_y = 0.79 \times 10^5$ rad/cm.

and π phase-shifted (antisymmetric) oscillations, respectively, in the unit cell. The E_{AS} mode is visible at large wave vectors q when the mode wavelength matches the one probed by BLS. In agreement with the experimental results, the PWM calculation shows that mode E exhibits a significant dispersion in the first BZ. The PWM provides a group velocity 2.6 km/s at $q_y = 0.05 \times 10^5$ rad/cm, being in good quantitative agreement with the measured value. We attribute the relatively large group velocity to a strong interaction between the edge excitations of neighboring holes which oscillate in phase. The strong coupling allows spin waves to propagate from hole to hole. The PWM thus substantiates deep-submicron SW channels between rows of holes [see mode E in Fig. 7(b)]. For the mode E, the PWM calculations predict the formation of a miniband that has not been resolved experimentally due to the low cross section of this mode for $q_y > 0.8 \times 10^5$ rad/cm. In contrast, the mode E_{AS} is almost independent on q in the first BZ. The out-of-phase edge modes between neighboring holes are much less coupled and, as a consequence, spin waves can not propagate.

From Fig. 7 we find that the rhombic lattice gives rise to numerous modes of different intensity at large f. Many of them exhibit only a small or vanishing slope $2\pi \frac{df}{dq}$ as a function of q_y. The BLS data reflect the most prominent ones exhibiting nearly constant eigenfrequencies. Still, there are discrepancies between the calculated and measured intensities of the modes at large f. We attribute these discrepancies to

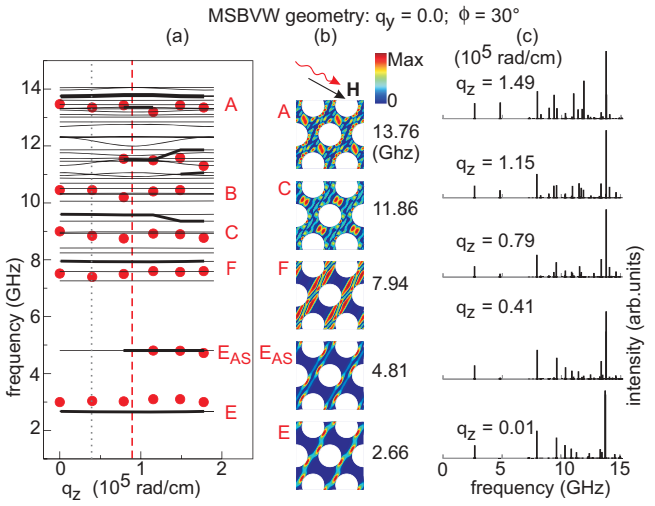

FIG. 8. (Color online) (a) Magnonic band structure in MSBVW geometry for $\phi = 30^\circ$ ($q_y = 0$). Circles represent peaks from BLS spectra. The thin lines are the PWM results. Bold lines emphasize the modes with large intensity calculated by PWM. The vertical dashed line marks the border of the first BZ (i.e., the M point) while the dotted line indicates the q vector where mode profiles of panel (b) have been calculated. (b) Maps show modulus of component m_x of the dynamical magnetization of modes E, E_{AS}, F, C, and A for $q_z = 0.41 \times 10^5$ rad/cm. (c) Relative values of BLS intensities calculated by PWM for different values q_z (values are given in units of 10^5 rad/cm). The intensity of mode E_{AS} is close to zero near the BZ center and starts to appear at $q_z = 0.41 \times 10^5$ rad/cm. Then, its intensity increases with increasing q_z. In BLS spectra, mode E_{AS} starts to be visible only around 1.15×10^5 rad/cm.

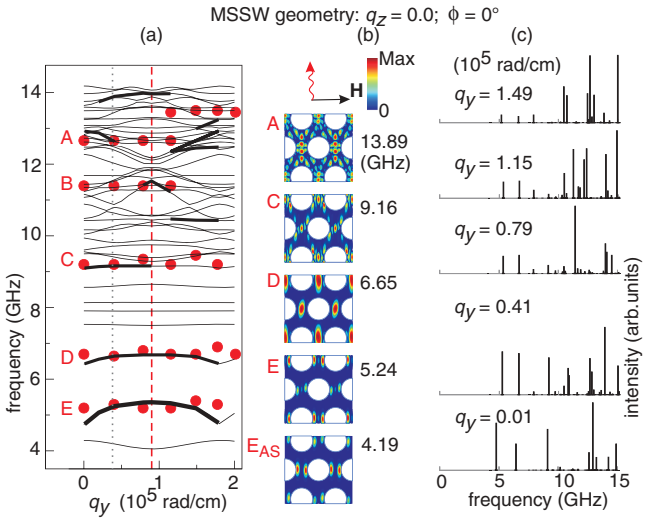

FIG. 9. (Color online) (a) Magnonic band structure in MSSW geometry for $\phi = 0^\circ$ ($q_z = 0$). Circles represent peaks of the BLS spectra. The thin lines are the PWM results. Bold lines emphasize modes with large intensity calculated by PWM. The vertical dashed line marks the border of the first BZ (i.e., the M point) while the dotted line indicates the q vector where mode profiles of panel (b) have been calculated. (b) Maps show modulus of the component m_x of the dynamic magnetization vector for $\phi = 0^\circ$ and $q_y = 0.41 \times 10^5$ rad/cm for modes E_{AS}, E, D, C, and A. Modes E_{AS} and E are edge excitations of different symmetry. Mode D has a spin-precession profile resembling mode D found in micromagnetic simulations. (c) Relative values of BLS intensities predicted by PWM for different values of q_y given in units of 10^5 rad/cm. There is a good agreement between PWM and BLS data for the edge excitations: mode E_{AS} is extremely weak, while mode E has a significant intensity.

the approximations made in the PWM calculations, where we assumed magnetic saturation all over the ADL and neglected the components of the static demagnetizing field that were perpendicular to the external magnetic field.

2. *MSBVW geometry for $\phi = 30^\circ$ with $q_z \neq 0$*

In Fig. 8(a), the experimental and calculated frequencies are depicted for the MSBVW geometry for $\phi = 30^\circ$. In this geometry, nearly all the modes exhibit a q independent eigenfrequency, i.e., they are quantized. In Fig. 8(b), we show the modulus of the amplitude of the x component of the dynamical magnetization vector for the most intense modes at $q_z = 0.41 \times 10^5$ rad/cm. From Figs. 8(a) and 8(b), we find that the edge excitations (mode E) do not couple significantly for **q** being perpendicular to the SW nanochannels. In Fig. 8(b), we see that the amplitude of the mode A is concentrated between holes along the direction perpendicular to **H**. This spin-precession profile is consistent with micromagnetic simulations for mode A shown in Fig. 2(b). The mode is the most intense one for small values of q_z [see Fig. 8(c)], but starting at $q_z \approx 1.78 \times 10^5$ rad/cm the intensity of the mode C becomes comparable. Mode C is similar to mode A, but with one nodal plane along **H**. This means that this mode can be interpreted as a higher-order magnetostatic backward volume wave, thereby residing at smaller eigenfrequency.

3. *MSSW geometry for $\phi = 0^\circ$ with $q_y \neq 0$*

For wave vectors q_y perpendicular to **H** applied along the z axis, the dispersion relation $f(q)$ exhibits mirror symmetry with respect to the boundary of the first BZ at $\phi = 0^\circ$. The PWM results (lines) are superimposed on the measured BLS frequencies (circles) in Fig. 9(a). The magnonic bands with large scattering cross section are emphasized by bold lines. In Fig. 9(c) relative intensities calculated by PWM are presented.

The spin-precession profiles of modes with most intense peaks for $q_y = 0.41 \times 10^5$ rad/cm are shown in Fig. 9(b). The edge excitations forming the low-frequency mode E_{AS} are found to precess out of phase. The scattering cross section is small and, consistently, mode E_{AS} is not detected by BLS in the whole wave vector range explored. The next higher lying mode E has a nonzero peak in the BLS spectra consistent with the large intensity predicted by the PWM [bold line in Fig. 9(a)]. The PWM predicts mode E to form a narrow allowed miniband with the frequency minimum at $q = 0$ and frequency maximum at the BZ boundary. However, the BLS data show more or less a constant eigenfrequency as a function of q_y. Numerous further modes of weak intensities are predicted by the PWM. They give rise to an involved band structure at high frequencies with several crossings and avoided crossings. The modes detected by BLS exhibit almost no variation with q.

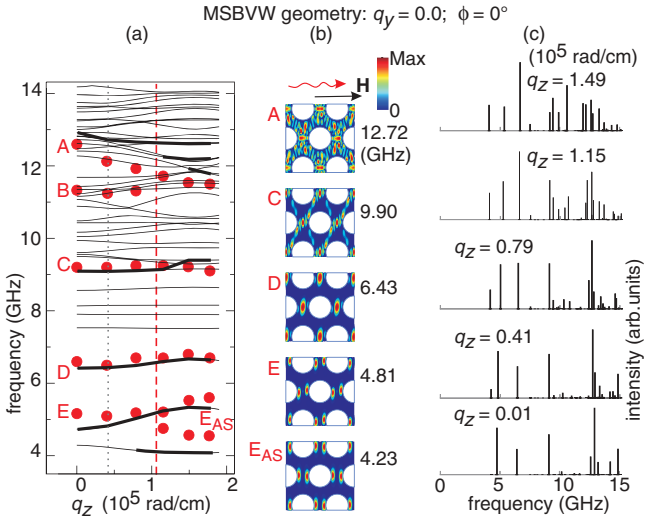

FIG. 10. (Color online) (a) Magnonic band structure in MSBVW geometry ($q_y = 0$) for $\phi = 0°$. Circles represent the points from the BLS measurements, the thin lines are the PWM results. Bold lines emphasize the modes with high intensity as calculated in PWM. The vertical dashed line marks the border of the first BZ (i.e., the K point) while the dotted line indicates the q vector where mode profiles of panel (b) have been calculated. (b) Maps show modulus of the dynamic component m_x for $\phi = 0°$ and $q_z = 0.41 \times 10^5$ rad/cm for the most intense SW modes: E_{AS}, E, D, C, and A. (c) Relative values of BLS intensities calculated using the PWM for SWs propagating along the z axis for different values of q_z given in units of 10^5 rad/cm.

4. *MSBVW geometry for $\phi = 0°$ with $q_z \neq 0$*

Calculated magnonic band structure and BLS intensities are shown in Figs. 10(a) and 10(c), respectively, considering the MSBVW geometry at $\phi = 0°$. Interestingly, a low-frequency mode appears in the BLS spectra for $q_z > 1.0 \times 10^5$ rad/cm and a frequency below 5 GHz. The observation of this low-frequency mode is consistent with PWM intensity calculations which predict an increasing intensity [see Fig. 10(c)] for this mode when q_z is larger that 10^5 rad/cm. Inspection of the spatial profile for this mode indicates that it is localized close to the hole edges and exhibits an antisymmetric character. This explains why it is visible only in the large wave vector range where the mode wavelength matches the one of the probing laser light.

The BLS data [see Fig. 10(a)] show a constant eigenfrequency for most of the modes. Only mode A (at about 12.5 GHz at $q_z = 0$) exhibits a (negative) slope with increasing q_z. The PWM predicts such a branch at a slightly higher frequency. A miniband behavior is not found. The mode crosses the BZ boundary q_{BZ} with a nearly constant slope. Spin-precession profiles of selected modes in MSBVW geometry for $\phi = 0°$ are presented in Fig. 10(b).

VI. CONCLUSIONS

We have reported SW modes in a periodic array of nanoholes forming a rhombic antidot lattice in a thin permalloy film. Using the PWM, we have substantiated spin wave propagation via coherently coupled edge excitations. Applying **H** at $\phi = 30°$, the rhombic ADL supports a propagating MSSW mode (mode E). The mode experiences a positive group velocity that is in good agreement with the result of PWM calculations, which resides in a 96-nm-wide channel formed by neighboring holes. Propagating spin waves in such extremely deep-submicron channels have not been reported when nano-optics with spin waves was discussed.[53] Only recently, sub-100-nm spin wave channels were observed in permalloy nanowires exhibiting a zigzaglike magnetic configuration.[54,55] Though, in the antidot lattice, the internal field has a periodic variation along the propagation direction and a full magnonic miniband has been predicted by the PWM calculations, the miniband behavior has not been experimentally observed. This is different to the coupled edge excitations recently found in a square lattice of holes.[11] The PWM allows us to explain the absence of a magnonic miniband by symmetry arguments of the reciprocal space of the rhombic lattice and by cross-section calculations. Propagation does not occur for a wave vector **q** *parallel* to **H** at $\phi = 30°$, i.e., perpendicular to the SW nanochannels. The nanochannels do not seem to couple across the rows of holes. When the angle is changed to $\phi = 0°$, the slope of $f(q)$ is significantly reduced for mode E in both scattering geometries. The BLS data provide $v_g \approx 0$. By changing the angle from one to the other high-symmetry direction, the propagation is thus suppressed. The high-frequency mode A is found to exhibit propagation with a negative v_g only for the complementary high-symmetry direction compared to mode E.

Aside from the good agreement between PWM and BLS data for the low-frequency edge modes, there is a quantitative difference in BLS intensities for the modes with higher frequencies. We think that the source of this discrepancy lays in assumptions of the PWM. Here, we assume a uniform magnetization and neglect components of the static demagnetizing field perpendicular to **H**. Both assumptions are connected with each other as the demagnetizing field provokes locally a rotation of magnetic moments away from the direction of the bias field.

In conclusion, we have shown that rhombic antidot lattices open novel perspectives for spin wave guiding. Spin waves of both, positive and negative group velocities propagate through the lattice. These dynamic properties are relevant for the research field of magnonics where transmission and modification of spin waves are considered for magnetic nanodevices operating in the GHz frequency regime.

ACKNOWLEDGMENTS

The authors thank Thomas Rapp for experimental support. This work was supported by the *Deutsche Forschungsgemeinschaft* via the German Excellence Cluster *Nanosystems Initiative Munich (NIM)*, the European Community's Seventh Framework Programme (FP7/2007-2013) under Grant Agreements Nos. 228673 (MAGNONICS) and 233552 (DYNAMAG), and the National Research Foundation (NRF), Singapore, under Grant No. NRFG-CRP 2007-05.

APPENDIX

The matrix $\hat{M}$ of the eigenvalue problem (9) can be written in a block-matrix form:

$$\hat{M} = \begin{pmatrix} \hat{M}^{xx} & \hat{M}^{xy} \\ \hat{M}^{yx} & \hat{M}^{yy} \end{pmatrix}. \quad \text{(A1)}$$

The submatrices in Eq. (A1) are defined as follows:

$$\hat{M}_{ij}^{xx} = -\hat{M}_{ij}^{yy} = -i\frac{q_y + G_{y,j}}{H|\mathbf{q}+\mathbf{G}_j|} S(\mathbf{q}+\mathbf{G}_j) M_S(\mathbf{G}_i - \mathbf{G}_j), \tag{A2}$$

$$\hat{M}_{ij}^{xy} = \delta_{ij} + \sum_l \frac{(\mathbf{q}+\mathbf{G}_j)\cdot(\mathbf{q}+\mathbf{G}_l)}{H} l_{ex}^2(\mathbf{G}_l - \mathbf{G}_j) M_S(\mathbf{G}_i - \mathbf{G}_l) + \frac{(q_y + G_{y,j})^2}{H|\mathbf{q}+\mathbf{G}_j|^2}[1 - C(\mathbf{q}+\mathbf{G}_j, x] M_S(\mathbf{G}_i - \mathbf{G}_j)$$
$$- \frac{(G_{z,i} - G_{z,j})^2}{H|\mathbf{G}_i - \mathbf{G}_j|^2} M_S(\mathbf{G}_i - \mathbf{G}_j)[1 - C(\mathbf{G}_i - \mathbf{G}_j, x)], \tag{A3}$$

$$\hat{M}_{ij}^{xy} = -\delta_{ij} - \sum_l \frac{(\mathbf{q}+\mathbf{G}_j)\cdot(\mathbf{q}+\mathbf{G}_l)}{H} l_{ex}^2(\mathbf{G}_l - \mathbf{G}_j) M_S(\mathbf{G}_i - \mathbf{G}_l) - \frac{1}{H} C(\mathbf{q}+\mathbf{G}_j, x) M_S(\mathbf{G}_i - \mathbf{G}_j)$$
$$+ \frac{(G_{z,i} - G_{z,j})^2}{H|\mathbf{G}_i - \mathbf{G}_j|^2} M_S(\mathbf{G}_i - \mathbf{G}_j)[1 - C(\mathbf{G}_i - \mathbf{G}_j, x)], \tag{A4}$$

where indexes of reciprocal lattice vectors i, j, and l are integer-numbered reciprocal lattice vectors. The additional functions used in the equations above are defined as follows:

$$S(\mathbf{q}, x) = \sinh(|\mathbf{q}|x) e^{-|\mathbf{q}|d/2}, \quad C(\mathbf{q}, x) = \cosh(|\mathbf{q}|x) e^{-|\mathbf{q}|d/2}. \tag{A5}$$

*grundler@ph.tum.de

[1] J. Jorzick, S. O. Demokritov, B. Hillebrands, M. Bailleul, C. Fermon, K. Y. Guslienko, A. N. Slavin, D. V. Berkov, and N. L. Gorn, Phys. Rev. Lett. **88**, 047204 (2002).

[2] S. L. Vysotski, S. A. Nikitov, and Y. A. Filimonov, J. Exp. Theor. Phys. **101**, 547 (2005).

[3] C. Yu, M. J. Pechan, W. A. Burgei, and G. J. Mankey, J. Appl. Phys. **95**, 6648 (2004).

[4] M. Yu, L. Malkinski, L. Spinu, W. Zhou, and S. Whittenburg, J. Appl. Phys. **101**, 09F501 (2007).

[5] O. N. Martyanov, V. F. Yudanov, R. N. Lee, S. A. Nepijko, H. J. Elmers, R. Hertel, C. M. Schneider, and G. Schönhense, Phys. Rev. B **75**, 174429 (2007).

[6] M. J. Pechan, C. Yu, R. L. Compton, J. P. Park, and P. A. Crowell, J. Appl. Phys. **97**, 10J903 (2005).

[7] S. McPhail, C. M. Gürtler, J. M. Shilton, N. J. Curson, and J. A. C. Bland, Phys. Rev. B **72**, 094414 (2005).

[8] M. Kostylev, G. Gubbiotti, G. Carlotti, C. Socino, S. Tacchi, C. Wang, N. Singh, A. Adeyeye, and R. L. Stamps, J. Appl. Phys. **103**, 07C507 (2008).

[9] H. Ulrichs, B. Lenk, and M. Münzenberg, Appl. Phys. Lett. **97**, 092506 (2010).

[10] C.-L. Hu, R. Magaraggia, H.-Y. Yuan, C. S. Chang, M. Kostylev, D. Tripathy, A. O. Adeyeye, and R. L. Stamps, Appl. Phys. Lett. **98**, 262508 (2011).

[11] S. Neusser, G. Duerr, S. Tacchi, M. Madami, M. Sokolovskyy, G. Gubbiotti, M. Krawczyk, and D. Grundler, Phys. Rev. B **84**, 094454 (2011).

[12] S. Neusser, B. Botters, M. Becherer, D. Schmitt-Landsiedel, and D. Grundler, Appl. Phys. Lett. **93**, 122501 (2008).

[13] G. Ctistis, E. Papaioannou, P. Patoka, J. Gutek, P. Fumagalli, and M. Giersig, Nano Lett. **9**, 1 (2009).

[14] S. Neusser, B. Botters, and D. Grundler, Phys. Rev. B **78**, 054406 (2008).

[15] S. Neusser and D. Grundler, Adv. Mater. **21**, 2927 (2009).

[16] S. Tacchi, M. Madami, G. Gubbiotti, G. Carlotti, A. O. Adeyeye, S. Neusser, B. Botters, and D. Grundler, IEEE Trans Magn. **46**, 172 (2010).

[17] S. Neusser, G. Duerr, H. Bauer, S. Tacchi, M. Madami, G. Woltersdorf, G. Gubbiotti, C. H. Back, and D. Grundler, Phys. Rev. Lett. **105**, 067208 (2010).

[18] G. Duerr, M. Madami, S. Neusser, S. Tacchi, G. Gubbiotti, G. Carlotti, and D. Grundler, Appl. Phys. Lett. **99**, 202502 (2011).

[19] R. Zivieri, S. Tacchi, F. Montoncello, L. Giovannini, F. Nizzoli, M. Madami, G. Gubbiotti, G. Carlotti, S. Neusser, G. Duerr, and D. Grundler, Phys. Rev. B **85**, 012403 (2012).

[20] A. Vovk, L. Malkinski, V. Golub, S. Whittenburg, C. O'Connor, J.-S. Jung, and S.-H. Min, J. Appl. Phys. **97**, 10J506 (2005).

[21] A. Barman, J. Phys. D: Appl. Phys. **43**, 195002 (2010).

[22] V. N. Krivoruchko and A. I. Marchenko, J. Appl. Phys. **109**, 083912 (2011).

[23] S. Tacchi, M. Madami, G. Gubbiotti, G. Carlotti, A. O. Adeyeye, S. Neusser, B. Botters, and D. Grundler, IEEE Trans Magn. **46**, 1440 (2010).

[24] V. V. Kruglyak, S. O. Demokritov, and D. Grundler, J. Phys. D: Appl. Phys. **43**, 264001 (2010).

[25] G. Gubbiotti, S. Tacchi, M. Madami, G. Carlotti, A. O. Adeyeye, and M. Kostylev, J. Phys. D: Appl. Phys. **43**, 264003 (2010).

[26] B. Lenk, H. Ulrichs, F. Garbs, and M. Münzenberg, Phys. Rep. **507**, 107 (2011).

[27] G. Carlotti and G. Gubbiotti, J. Phys. C **14**, 8199 (2002).

[28] Z. K. Wang, H. S. Lim, V. L. Zhang, J. L. Goh, S. C. Ng, M. H. Kuok, H. L. Su, and S. L. Tang, Nano Lett. **6**, 1083 (2006).

[29] S. Choi, K.-S. Lee, K. Y. Guslienko, and S.-K. Kim, Phys. Rev. Lett. **98**, 087205 (2007).

[30] K.-S. Lee, D.-S. Han, and S.-K. Kim, Phys. Rev. Lett. **102**, 127202 (2009).

[31] Z. K. Wang, V. L. Zhang, H. S. Lim, S. C. Ng, M. H. Kuok, S. Jain, and A. O. Adeyeye, ACS Nano **4**, 643 (2010).

[32] A. Khitun, M. Bao, and K. L. Wang, J. Phys. D: Appl. Phys. **43**, 264005 (2010).

[33]C. C. Wang, A. O. Adeyeye, and N. Singh, Nanotechnology **17**, 1629 (2006).
[34]J. Podbielski, F. Giesen, M. Berginski, N. Hoyer, and D. Grundler, Superlattices Microstruct. **37**, 341 (2005).
[35]S. S. Kalarickal, P. Krivosik, M. Wu, C. E. Patton, M. L. Schneider, P. Kabos, T. J. Silva, and J. P. Nibarger, J. Appl. Phys. **99**, 093909 (2006).
[36]M. Belmeguenai, T. Martin, G. Woltersdorf, G. Bayreuther, V. Baltz, A. K. Suszka, and B. J. Hickey, J. Phys.: Condens. Matter **20**, 345206 (2008).
[37]B. Botters, F. Giesen, J. Podbielski, P. Bach, G. Schmidt, L. Molenkamp, and D. Grundler, Appl. Phys. Lett. **89**, 242505 (2006).
[38]M. Bailleul, D. Olligs, C. Fermon, and S. O. Demokritov, Europhys. Lett. **56**, 741 (2001).
[39]G. Counil, J.-V. Kim, T. Devolder, C. Chappert, K. Shigeto, and Y. Otani, J. Appl. Phys. **95**, 5646 (2004).
[40]V. Vlaminck and M. Bailleul, Phys. Rev. B **81**, 014425 (2010).
[41]S. Tacchi, M. Madami, G. Carlotti, G. Gubbiotti, M. Marangolo, J. Milano, R. Breitwieser, V. H. Etgens, R. L. Stamps, and M. G. Pini, Phys. Rev. B **80**, 155427 (2009).
[42]D. V. Berkov and N. L. Gorn, http://www.micromagus.de, software package for micromagnetic simulations.
[43]J. D. Joannopoulos, S. G. Johnson, J. N. Winn, and R. D. Meade, *Photonic Crystals: Molding the Flow of Light*, 2nd ed. (Princeton University Press, Princeton, 2008).
[44]D. W. Prather, S. Shi, A. Sharkawy, J. Murakowski, and G. J. Schneider, *Photonic Crystals: Theory, Applications, and Fabrication* (Wiley, 2009).
[45]V. Laude, M. Wilm, S. Benchabane, and A. Khelif, Phys. Rev. E **71**, 036607 (2005).
[46]M. Krawczyk and H. Puszkarski, Phys. Rev. B **77**, 054437 (2008).
[47]J. O. Vasseur, P. A. Deymier, B. Djafari-Rouhani, Y. Pennec, and A.-C. Hladky-Hennion, Phys. Rev. B **77**, 085415 (2008).
[48]R. P. Tiwari and D. Stroud, Phys. Rev. B **81**, 220403(R) (2010).
[49]A. Raman and S. Fan, Phys. Rev. Lett. **104**, 087401 (2010).
[50]M. Sokolovskyy and M. Krawczyk, J. Nanopart. Res. **13**, 6085 (2011).
[51]J. W. Klos, M. Krawczyk, and M. L. Sokolovskyy, J. Appl. Phys. **109**, 07D311 (2011).
[52]C. Mathieu, J. Jorzick, A. Frank, S. O. Demokritov, A. N. Slavin, B. Hillebrands, B. Bartenlian, C. Chappert, D. Decanini, F. Rousseaux, and E. Cambril, Phys. Rev. Lett. **81**, 3968 (1998).
[53]V. E. Demidov, S. O. Demokritov, K. Rott, P. Krzysteczko, and G. Reiss, Appl. Phys. Lett. **92**, 232503 (2008).
[54]J. Topp, J. Podbielski, D. Heitmann, and D. Grundler, Phys. Rev. B **78**, 024431 (2008).
[55]D. Duerr, K. Thurner, J. Topp, R. Huber, and D. Grundler, Phys. Rev. Lett. **108**, 227202 (2012).
[56]R. E. Camley, P. Grünberg, and C. M. Mayr, Phys. Rev. B **26**, 2609 (1982).
[57]Recently we have introduced imperfections in the simulations (unpublished). They move up the eigenfrequency, but do not change the overall spin precession profile used here to explain the mode.
[58]At room temperature, Stokes and anti-Stokes scattering processes which correspond to the creation and annihilation of a magnon, respectively, possess the same probability. However, there are factors which influence the relative intensity of peaks provoking a large asymmetry in the Stokes and anti-Stokes side of the spectrum. Among them, there are the localization of modes close to the upper or lower surface of a ferromagnet, interference effects and the finite ellipticity of the precessional magnetization trajectory.[56] We did not label all peaks in the spectra to avoid overcrowding of labels.
[59]The static demagnetizing field in the model system must reproduce well the demagnetizing and stray fields in the real ADL. The calculations performed indicate that the assumption of a saturation magnetization value at least ten times lower than that in Py allows to reproduce the profile and magnitude of the static demagnetizing field with good accuracy (less than 10% error). The assumption of a specific value of saturation magnetization involves a compromise between the accuracy of the results and the required calculation time.